Diabolical touching point in the magnetic energy levels of topological nodal-line metals

Chong Wang,[1,*] Zhongyi Zhang,[2,*] Liqin Zhou,[2] Hongming Weng,[2] Chen Fang,[2,†] and A. Alexandradinata[3,‡]
[1]*Department of Physics, Carnegie Mellon University, Pittsburgh, Pennsylvania 15213, USA*
[2]*Institute of Physics, Chinese Academy of Sciences, Beijing 100080, China*
[3]*Department of Physics and Institute for Condensed Matter Theory, University of Illinois at Urbana-Champaign, Urbana, Illinois 61801, USA*

(Received 21 February 2021; revised 17 October 2021; accepted 12 January 2022; published 28 January 2022)

For three-dimensional metals, Landau levels disperse as a function of the magnetic field and the momentum wave number parallel to the field. In this two-dimensional parameter space, it is shown that two conically dispersing Landau levels can touch at a diabolical point—a *Landau-Dirac point*. The conditions giving rise to Landau-Dirac points are shown to be magnetic breakdown (field-driven quantum tunneling) and certain crystallographic spacetime symmetry. Both conditions are realizable in topological nodal-line metals, as we exemplify with the material candidates CaX_3 (X = As, P). The experimental fingerprints of a Landau-Dirac point include (a) anomalous "batman"-like peaks in the magnetoresistance, (b) circular Landau-Fermi surfaces revealed by angle-dependent ultrasonic attenuation, and (c) the tunability of the frequency onset of optical absorption to zero.

DOI: 10.1103/PhysRevB.105.045141

For a real Hamiltonian, energy-level surfaces over a two-dimensional parameter space can locally form a double cone (*diabolo*) with an energy-degenerate vertex known as a *diabolical point* [1–4]. The first physical application of the diabolical point was by Hamilton in his 1832 prediction of conical refraction [5,6]. Since then, the diabolical point has re-emerged in diverse phenomena in singular optics [7], chemistry [8–10], and nuclear [11] and quantum [12] physics. Its most recent revival is as Dirac-Weyl points [13] in the crystal-momentum space of topological semimetals [14–18] and insulators [19–22].

This work presents another type of diabolical point in a textbook solid-state phenomenon: the quantized energy spectrum of three-dimensional metals subject to a homogeneous magnetic field. A fundamental feature of the magnetic energy spectrum is its quantization into Landau levels [23], which are naturally parametrized by the field magnitude (B) and the momentum wave number (k_z) parallel to the field. In this two-dimensional parameter space, Fig. 1(b) illustrates how two Landau-level surfaces can touch at a diabolical point, which will be referred to as a *Landau-Dirac point*. Parallel transport around an equienergy contour of the Landau-Dirac cone gives a topologically quantized, π Berry phase [24].

Landau-Dirac points do *not* exist for metals with a single Fermi pocket; their Landau levels are determined by the Onsager-Lifshitz-Roth quantization rule [25–27]: $\hbar/eB = (2\pi n+\gamma)/S(E,k_z)$, with $S(E,k_z)$ the $\boldsymbol{k}$ area enclosed by the orbit, $0 \leqslant n \in \mathbf{Z}$ the Landau-level index, and $\gamma \approx 1$ being field independent to leading order in B [27–30]. Henceforth, we set $\hbar = e = 1$ so that B^{-1} equals the square of the magnetic length. Generally for an electron-like (resp. hole-like) pocket, $S(E,k_z)$ is a single-valued function of k_z and an increasing (resp. decreasing) function of energy E, e.g., $S = \pi(2mE - k_z^2)$ for a free-electron gas with mass m. These conditions on $S(E,k_z)$ ensure that equienergy solutions of the quantization rule lie on *open*, nonintersecting contours in (B^{-1}, k_z) space, as illustrated for the free-electron gas in Fig. 1(a). It follows that the *closed* equienergy contours of the diabolo [cf. Fig. 1(b)] cannot derive from a single electron-like or hole-like pocket.

However, if multiple pockets are linked by field-driven quantum tunneling (known as magnetic breakdown [31–35]), we will show that tunneling-induced level repulsion can convert open contours to closed contours of a diabolo. A stable Landau-Dirac point relies on certain crystallographic symmetries that are preserved in the presence of the field. For example, the composition $T\mathfrak{c}_{2y}$ of time reversal and twofold rotation (about a field-orthogonal axis) maps $(B^{-1},k_z)\rightarrow(B^{-1},k_z)$, ensuring that Landau-Dirac points are movable over (B^{-1},k_z) space, but irremovable unless annihilated in pairs—as analogous to Dirac points in graphene [15]. Either spatial inversion $\mathfrak{i}$ $[(x,y,z)\rightarrow(-x,-y,-z)]$ or reflection $\mathfrak{r}_z$ $[(x,y,z)\rightarrow(x,y,-z)]$ maps $(B^{-1},k_z)\rightarrow(B^{-1},-k_z)$, and therefore protects crossings between Landau levels of opposite $\mathfrak{i}$ (or $\mathfrak{r}_z$) representations on high-symmetry lines. All three symmetries, plus the condition of magnetic breakdown, are realizable in topological nodal-line metals [36–41], as we will first demonstrate with a conceptually simple, minimal model, and subsequently for the nodal-line metallic candidates CaX_3 (X = As, P). We will show further that a Landau-Dirac point reveals itself in anomalous "batman"-like peaks in the density of states [cf. Fig. 1(b)], as well as having unique fingerprints in ultrasonic attenuation and optical absorption.

*These authors contributed equally to this work.
†cfang@iphy.ac.cn
‡aalexan7@illinois.edu

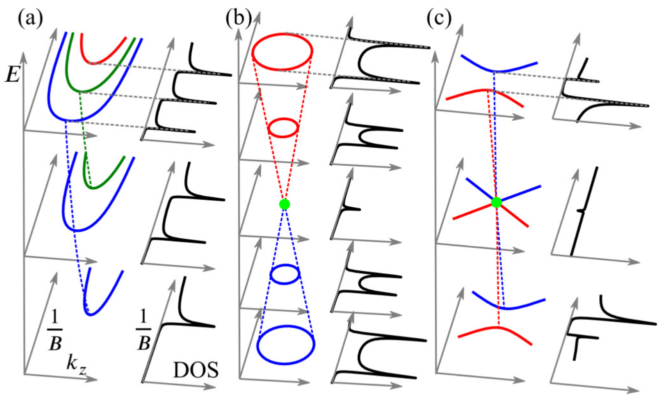

FIG. 1. Magnetic energy levels for a free-electron gas (a), and for topological nodal-line metals [(b), (c)]. Left of each panel: equienergy contours of energy-level surfaces in (B^{-1}, k_z) space, with distinct surfaces distinguished by color; right: corresponding density of states, regularized by a finite lifetime.

I. PROOF OF PRINCIPLE

We first present a minimal model of Landau-Dirac points with both $\mathfrak{r}_z$ and $T\mathfrak{c}_{2y}$ symmetries. At zero field, our effective-mass model describes two parabolic bands with opposite-sign masses:

$$H(\boldsymbol{k}) = \left[\left(k_x^2 + k_y^2\right)/2m - \varepsilon_0\right]\tau_3 + u_z k_z \tau_1 + u_x k_x. \quad (1)$$

$\varepsilon_0 > 0$ implies that the two bands overlap on the energy axis; however, level repulsion is absent in the $k_z = 0$ plane owing to $\mathfrak{r}_z$ symmetry: $\tau_3 H(\boldsymbol{k})\tau_3 = H(k_x, k_y, -k_z)$. It follows that a zero-energy, nodal-line degeneracy encircles $\boldsymbol{k} = \boldsymbol{0}$ with radius $k_R = \sqrt{2m\varepsilon_0}$, supposing $u_x = 0$. If nonzero, the $u_x k_x$ term causes the nodal line to disperse with bandwidth $\Delta E = 2u_x k_R$. Thus, for a Fermi energy satisfying $|E_F| < \Delta E/2$, the Fermi surface comprises electron and hole pockets that interconnect like a linked sausage, as illustrated in Fig. 2(b). Close to either interconnection points (with $E_F = 0$), an effective Hamiltonian is attained by linearizing Eq. (1) around $\boldsymbol{k} = (0, \pm k_R, 0)$:

$$H_\pm = \pm u_y \delta k_y \tau_3 + u_z k_z \tau_1 + u_x k_x, \quad u_y = \sqrt{2\varepsilon_0/m}, \quad (2)$$

whose equienergy contours form a hyperbola depicted in the inset of Fig. 2(a).

Applying a magnetic field parallel to $-z$, the magnetic energy levels are eigenvalues of the Peierls-Onsager Hamiltonian $H(K_x, K_y, k_z)$, which is obtained by substituting (k_x, k_y) in the zero-field Hamiltonian [cf. Eq. (1)] by noncommuting operators satisfying $[K_y, K_x] = iB$ [42,43]. If B is much smaller than the $\boldsymbol{k}$ area of both sausage-shaped pockets, the following semiclassical interpretation holds: The Lorentz force pushes electrons along trajectories indicated by arrows in Fig. 2(a). In the vicinity of both connection points [$\boldsymbol{k} = (0, \pm k_R, 0)$], interpocket tunneling occurs with the Landau-Zener probability [33,44–51]:

$$\rho^2 = e^{-2\pi\mu}, \quad \mu = S_\square/8B, \quad S_\square = 4v_z^2 k_z^2/v_x v_y, \quad (3)$$

with $S_\square$ being the rectangular area inscribed by the two hyperbolic arms [cf. inset of Fig. 2(a)]. By matching the Wentzel-Kramers-Brillouin (WKB) wave functions [52] at the tunneling regions (by the Landau-Zener connection formula [49]), we derive a quantization rule for the magnetic energy levels:

$$0 = Q(E, k_z, B^{-1}) = \cos X + \rho^2 \cos Y + \tau^2 \cos Z,$$

$$(X, Y, Z) = \frac{1}{2B}(S_1 - S_3, S_{12} + S_{23}, S_1 + S_3 + 4\omega B), \quad (4)$$

with $\tau^2 = 1 - \rho^2$ being the probability that an incoming electron "reflects" off the tunneling region with a different velocity. $\omega = \mu - \mu \ln \mu + \arg[\Gamma(i\mu)] + \pi/4$ is the phase acquired during this adiabatic reflection, with Γ being the Gamma function; S_1 (S_3) is the $\boldsymbol{k}$ area of the left (right) sausage-shaped pocket, and $S_{12} := S_1 + S_2$ ($S_{23} := S_2 + S_3$) is the area of the left (right) circular trajectory linked by tunneling [cf. Fig. 2(a)].

For $k_z = \mu = 0$, Landau-Zener tunneling occurs with unit probability, and solutions of Eq. (4) describe independent cyclotron orbits over overlapping circles:

$$\cos X + \cos Y = 0 \;\Rightarrow\; S_{12,23}(E, 0)/B = 2\pi(n + 1/2). \quad (5)$$

The zero-energy solutions of Eq. (5) are doubly degenerate and lie at equidistant points on the vertical axis of Fig. 2(c), owing to the commensuration of areas: $S_{12}(0, k_z) = S_{23}(0, k_z)$, which derives from the effective-mass Hamiltonian in Eq. (1).

There is no unique semiclassical trajectory in the intermediate tunneling regime with nonzero, finite $\mu \propto k_z^2$. We focus on a class of solutions contained in certain hypersurfaces in (E, k_z, B^{-1}) space (r space, in short), defined by $X(r)/\pi \in 2\mathbb{Z}$ and $2\mathbb{Z} + 1$. Whether even or odd, $\cos X$ is extremized to ± 1, and hence this class of solutions satisfy $\cos Y = \cos Z = \mp \cos X$. These two constraints (within a two-dimensional hypersurface) can only be satisfied at isolated points, denoted by $\{\bar{r}\}$. Such points lying within the ($X = 0$) hypersurface

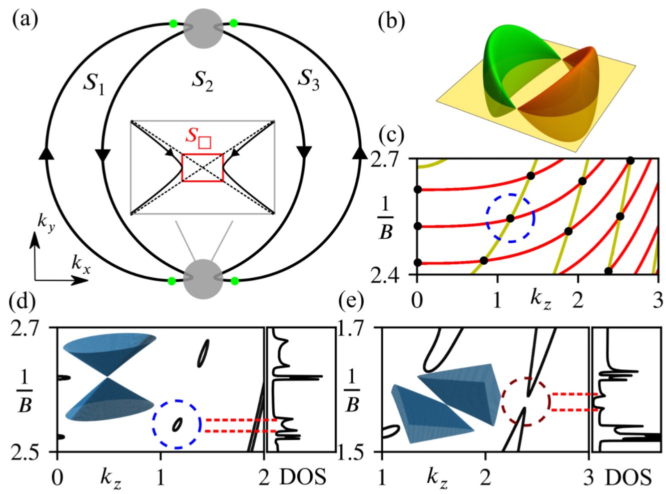

FIG. 2. For the minimal model in Eq. (1) with parameters $v_x = v_z = m = 1$ and $\epsilon_0 = 10$, we plot the zero-energy, Fermi surface within the Brillouin zone in panel (b); a constant ($k_z = 0.4$) cross section of the same surface is shown in panel (a). Inset of panel (a): enlarged view of breakdown region. Landau-Fermi surfaces over (B^{-1}, k_z) are indicated by black dots and black lines in panels (c)–(e), for E=0, 0.01, 0.95 respectively. Right panels [(d) and (e)] plot the corresponding density of states (DOS) in arbitrary units. The diabolo in panel (d) [(e)] is the energy dispersion of the type I (resp., type II) Landau-Dirac cone encircled in blue (resp., brown).

are illustrated as black dots in Fig. 2(c); note the $(X = 0)$ hypersurface is just the $E = 0$ plane owing to the just-mentioned commensuration condition, and the black dots lie at the intersections of red lines (defined by $\cos Y = -1$) and yellow lines ($\cos Z = -1$).

Moving off a hypersurface in the normal (or antinormal) direction, each point solution evolves into an ellipse, as illustrated for $E = 0.01$ in Fig. 2(d). To prove that $\bar{r}$ is a diabolical point, apply that $\bar{r}$ is an extremal point for each of $\{\cos X, \cos Y, \cos Z\}$. Consequently, for any solution of the quantization rule that deviates from $\bar{r}$ by small $\delta r = (\delta E, \delta k_z, \delta B^{-1})$, $0 = Q(\bar{r} + \delta r) - Q(\bar{r})$, with the right-hand side quadratic in δr to the lowest order. Solving this quadratic equation for the Landau-level dispersion,

$$\delta E = (-b \pm \sqrt{b^2 - 4ac})/2a, \quad a = X_E^2 - \rho^2 Y_E^2 - \tau^2 Z_E^2,$$
$$b = [2X_E(\delta k_z X_z + \delta B^{-1} X_{B^{-1}})] - \rho^2 [X \to Y] - \tau^2 [X \to Z],$$
$$c = [(\delta k_z X_z + \delta B^{-1} X_{B^{-1}})^2] - \rho^2 [X \to Y] - \tau^2 [X \to Z].$$

$X_{E,z,B^{-1}}$ denotes the partial derivative of X with respect to (E, k_z, B^{-1}), as evaluated at $\bar{r}$; $[X \to Y]$ denotes the substitution of X with Y in the square-bracketed expression on the same line. Since the quantity under the square root is quadratic in $(\delta k_z, \delta B^{-1})$, the solution in $(\delta k_z, \delta B^{-1})$ space generically forms a diabolo with vertex at $\bar{r}$.

The perturbative stability of Landau-Dirac points is guaranteed by $T\mathfrak{c}_{2y}$ symmetry: $H(K_x, K_y, k_z)^* = H(K_x, -K_y, k_z)$. Given this antiunitary constraint, a standard generalization [53] of the von Neumann–Wigner theorem [1] states that the codimension of an eigenvalue degeneracy is two, implying degeneracies are perturbatively stable in the two-dimensional (B^{-1}, k_z) space. The Landau-Dirac points at $k_z = 0$ are doubly protected by $\mathfrak{r}_z$ symmetry, because each such point is a crossing between levels in distinct eigenspaces of τ_3.

II. TYPE-II LANDAU-DIRAC POINTS

While the $(X = 0)$ hypersurface is the $E = 0$ plane, $(X = \pi j)$ hypersurfaces are increasingly dispersive for larger $|j|$. With sufficient dispersion, the conical axis tilts away from the energy axis, such that the diabolo [centered at $(\bar{E}, \bar{k}_z, \bar{B}^{-1})$] intersects the $E = \bar{E}$ plane on open lines; such a *type-II Landau-Dirac point* occurs if and only if $ac < 0$ on any segment of a circle encircling the diabolical point. A type-II point lying on the $X = 6\pi$ hypersurface is illustrated in Fig. 2(e).

An isolated, type-I point is distinguishable from type II by the Fermi-level density of states (DOS). The intersection of a magnetic band with the Fermi level defines a *Landau-Fermi surface* in $(1/B, k_z)$ space; in the type-I case, the Landau-Fermi surface is deformable to a circle, and can be parametrized by a multivalued function $B^{-1}(k_z)$ with two extrema. At each extremum, the DOS has a van Hove singularity that is left-right asymmetric, being proportional to $[\pm(B^{-1} - B_0^{-1})]^{-1/2}$ on one side of the singularity but not the other. (Such left-right asymmetry is routinely measurable in thermodynamic and galvanomagnetic experiments [54–56].) Figure 1 illustrates that the inverse-square-root "tails" (in a type-I scenario) trail toward each other, resembling the helm of Batman; conversely, type-II tails trail apart, like anti-Batman. For our minimal model in Eq. (1), we plot the DOS in the right panels of Figs. 2(d) and 2(e), with the correspondence between Batman peaks and type-I Landau-Fermi surfaces [resp. anti-Batman and type II] indicated by red dashed lines in Fig. 2(d) [resp. Fig. 2(e)]. Unlike conventional peaks in Schubnikov–de Haas–van Alphen oscillations, Batman peaks associated to quantum tunneling are generally *nonperiodic* in $1/B$; the width of the Batman helm is likewise *not* attributable to the area of any $\boldsymbol{k}$ loop in the graph.

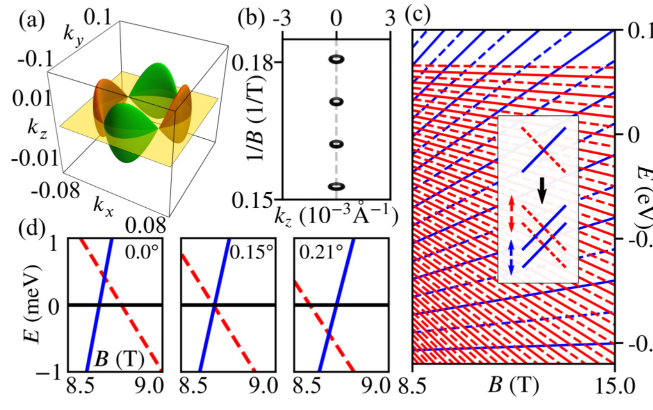

FIG. 3. For a $\boldsymbol{k}\cdot\boldsymbol{p}$ model [57] of CaP_3 without spin-orbit coupling, we plot (a) the Fermi surface, (b) Landau-Fermi surface, and (c) Landau-level dispersion at $k_z = 0$ and B parallel to z. Panel (d) shows the dispersion of a specific Landau-Dirac point, for B tilted within the xz plane by angles $\theta_B = 0^\circ,\ 0.15^\circ,\ 0.21^\circ$, with the electron density fixed throughout. Inset of panel (c) illustrates a spin-split Landau-Dirac point.

III. MATERIAL CASE STUDIES

The Landau-Dirac phenomenology potentially manifests in a number of topological-metallic candidates: $CaAs_3$ [58], CaP_3 [57], SrP_3 [57], and Ca_3P_2 [59,60], each of which has a Fermi surface enclosing a single, circular nodal line—just like our minimal model. For concreteness, we pick $P\bar{1}$-symmetric [61] CaX_3 (X = As, P) for our final case study. Its point group is generated solely by the spatial inversion $\mathfrak{i}$. CaX_3's nodal line is predicted [57,58] to be centered at an inversion-invariant wavevector on the BZ boundary, and encircles an area $\lesssim 1/50$ the areal dimension of the BZ—this allows for an accurate description by an effective-mass Hamiltonian $H(\boldsymbol{k}) = \sum_{i=0}^{3} d_i(\boldsymbol{k})\tau_i$, with τ_0 being the identity matrix; the two-by-two matrix structure reflects our (present) ignorance of the weak spin-orbit interaction.

Our effective-mass parameters (detailed in the Supplemental Material [62]) are chosen such that the Fermi surface consists of four interconnected pockets (two electron-like and two hole-like), as has been predicted for CaX_3 [57,58]. Owing to $\mathfrak{i}$ symmetry $[\tau_3 H(\boldsymbol{k})\tau_3 = H(-\boldsymbol{k})]$ and time-reversal symmetry (represented by complex conjugation), momentum coordinates can be chosen such that the interpocket connections lie in the $k_z = 0$ plane [cf. Fig. 3(a)] and $[H(k_x, k_y, k_z = 0), \tau_3] = 0$. This $U(1) \times U(1)$ symmetry encodes the nonmixing of orbitals indexed by $\langle\tau_3\rangle = \pm 1$.

The corresponding Landau levels (restricted to $k_z = 0$) are plotted in Fig. 3(c), with blue (red) lines indicating $\langle\tau_3\rangle = 1$ ($\langle\tau_3\rangle = -1$). For either $\langle\tau_3\rangle$, the $\mathfrak{i}$ eigenvalue alternates between adjacent levels [23], as illustrated by alternating solid ($\mathfrak{i}$-even) and dashed ($\mathfrak{i}$-odd) lines. Half of the Landau-Dirac points in Fig. 3(c) are $\mathfrak{i}$-protected crossings between solid and dashed lines; the other half are protected by $U(1) \times U(1)$ symmetry but not by $\mathfrak{i}$. For small $k_z \neq 0$, the four sausage links in Fig. 3(a) disconnect; electron dynamics in the vicinity of the four disconnected links is again of the Landau-Zener type, with tunneling probability $\exp(-2\pi\mu)$. The resultant Landau-Fermi surface form closed lobes encircling the type-I Landau-Dirac points at $k_z = 0$, as shown in Fig. 3(b).

Though our analysis has assumed a specific field orientation, half the crossings in Fig. 3(c) are perturbatively stable against tilting of the field, because $\mathfrak{i}$ symmetry is maintained for any field orientation; the other half that relies on $U(1) \times U(1)$ symmetry will destabilize.

We have thus far neglected spin in the CaX_3 study. Because the intrinsic Zeeman and spin-orbit interactions maintain $\mathfrak{i}$ symmetry, each spin-degenerate Landau level perturbatively splits in energy, converting a single, spin-degenerate, $\mathfrak{i}$-protected Landau-Dirac point into four, spin-nondegenerate, $\mathfrak{i}$-protected Landau-Dirac points, as illustrated in Fig. 3(c). Nonperturbatively, we expect the Landau-Dirac cones to persist so long as the spin-orbit energy is less than the dispersion bandwidth of the nodal line [cf. ΔE below Eq. (1)]; this is the regime where quantum tunneling remains relevant.

IV. EXPERIMENTAL DIAGNOSTICS

The experimental observation of Batman peaks in the magnetoresistance would be suggestive but not conclusive of a type-I Landau-Dirac cone. One must further demonstrate that both peaks originate from a single Landau-Fermi surface that is topologically equivalent to a circle in $(1/B, k_z)$ space [cf. Fig. 1(b)]. This relies on our ability to map out the entire Landau-Fermi surface, which we propose to accomplish by *angle-dependent ultrasound attenuation*. Our proposal generalizes existing ultrasound methodology [54,63,64] to measure "giant quantum oscillations" [65] in the $(1/B)$-dependent attenuation coefficient, for which the angle between sound wave vector and B field remains *fixed*. We propose here to ignore these oscillations and instead track *individual* peaks by varying both the B magnitude and the sound-wave vector orientation, with fixed B orientation.

When an electronic quasiparticle in a magnetic energy band [with dispersion $E_n(k_z, B)$] absorbs an acoustic phonon [with typical wavenumber $|\boldsymbol{q}| \approx (5\,\mu\text{m})^{-1}$], inter-Landau-level transitions are forbidden for B large enough that $|E_{n+1} - E_n| > 0.1$ meV. This inequality holds assuming that the magnetic velocity in the Taylor expansion

$$E_n(k_z + q_z, B) = E_n(k_z, B) + v_n(k_z, B)q_z + \frac{q_z^2}{2m_n(k_z, B)} + \cdots$$

satisfies $|v_n| \leqslant c/100$, and the magnetic mass $m_n > m_e/1000$ with m_e being the free-electron mass. Energy-momentum conservation requires that resonant sound absorption occurs only if the electron "rides the surf" of the sound-wave fronts [54,64], i.e., the $\boldsymbol{q}$-parallel component of the magnetic velocity $(v_n\boldsymbol{B}/|\boldsymbol{B}|)$ equals the sound speed s:

$$v_n(k_z, B_n)\cos(\theta) \approx s(\boldsymbol{q}/|\boldsymbol{q}|), \quad \cos\theta = \frac{\boldsymbol{B}}{|\boldsymbol{B}|}\cdot\frac{\boldsymbol{q}}{|\boldsymbol{q}|}. \tag{6}$$

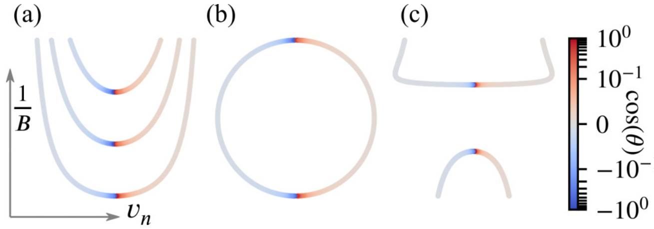

FIG. 4. For the highest equienergy contours of Figs. 1(a)–1(c), we plot $1/B$ vs the field-parallel Fermi velocity $v_n = dE_n/dk_z$ in panels (a)–(c), respectively. The color of the plotted lines indicate the direction cosine $\cos(\theta) \in [-1, 1]$ (of sound wave vector relative to B field) where resonant, ultrasound absorption occurs. We have assumed an isotropic sound speed s satisfying $s/\max(|v_n|) = 1/100$.

Pauli's exclusion principle requires that we evaluate v_n at $B = B_n$ where the nth Landau level crosses the Fermi level. Fixing $B = B_n$ and varying θ, resonant absorption occurs at an angle-dependent electronic wave number $k_{z;n} = k_z(\cos\theta, B_n, s)$ satisfying Eq. (6). By varying $\theta \in [0, \pi]$, $k_{z;n}$ covers essentially the entire Landau-Fermi surface; only a tiny fraction $(\sim s/\max(|v_n|) \lesssim 10^{-2})$ of the surface is missed for k_z values where $v_n \lesssim s$, and Eq. (6) cannot be satisfied. In practice, θ is varied by gluing piezoelectric transducers [63] to multiple crystal facets cut by wire or focused ion beam [66], with the facet orientation determined by x-ray diffraction. Figure 4 illustrates how this technique is able, in principle, to distinguish the Landau-Fermi surfaces associated to free electrons, type-I and type-II Landau-Dirac cones: The reconstructed surfaces over $(1/B, v_n)$ are topologically equivalent to the Landau-Fermi surfaces over $(1/B, k_z)$.

We have assumed in Fig. 4 the generic scenario in which the Landau-Dirac point lies away from the Fermi level. Otherwise, inter-Landau-level transitions may occur with Eq. (6) failing to hold. Two tunable parameters are needed to bring an $\mathfrak{i}$- or $\mathfrak{r}_z$-protected Landau-Dirac point to the Fermi level, e.g., by tuning B^{-1}, the two Landau levels (closest to the Fermi level) can be made to cross; by tuning the B-tilt angle θ_B, such crossing can be brought to the Fermi level, as illustrated in Fig. 3(d) for the CaX_3 model.

To directly diagnose a Landau-Dirac *point*, we propose that the frequency onset of optical absorption *linearly* evolves to zero as a function of θ_B. Such an optical transition between Landau levels of distinct $\mathfrak{i}$ representations is allowed by the dipole selection rule [67]. Optical experiments in the far-infrared, submillimeter-wavelength regime [68–70] have a penetration depth $\lambda \approx 100$ nm in many metals [71] λ greatly exceeding the magnetic length $[25\text{ nm}/\sqrt{B\,(T)}]$ for $B \approx 10\,T$ allows for optical excitations to directly reflect bulk, inter-Landau-level transitions.

V. DISCUSSION

We have shown how the diabolical point in solid-state, magnetic energy levels originates from quantum tunneling; an individual Landau-Dirac point is topologically irremovable if certain magnetic space-group symmetries are preserved. Topological nodal-line metals provide an ideal experimental platform to realize Landau-Dirac points. *Ab initio* calculations have predicted that CaX_3 is either a band-inverted topological metal, or can be band inverted under lattice compression [57,58,72]. The existence of a nodal line in $CaAs_3$ is as yet inconclusive, but would be corroborated by observing the Landau-Dirac phenomenology proposed in this work.

Future investigations would determine if a similar phenomenology exists for two other topological-nodal-line material candidates, which host more complicated Fermi surfaces than the present study: (a) $SrAs_3$ has an experimentally evidenced [73–75], nodal-line degeneracy, and (b) the square-net compound ZrSiS is known to undergo magnetic breakdown [76]. While $SrAs_3$ is chemically similar to $CaAs_3$, the former has an additional, twofold rotational symmetry that protects nodal-*line* degeneracies in (B^{-1}, k_z) space, if the field is oriented along the twofold axis.

ACKNOWLEDGMENTS

We thank Di Xiao and Yang Gao for insightful theoretical discussions. We are also indebted to Philip Moll, Jinghui Wang, Wei Xia, and Changjiang Yi for discussions of possible candidate materials. Brad Ramshaw and Clemens Schindler gave expert advice on ultrasound techniques. C.W. was supported by the Department of Energy, Basic Energy Sciences, Materials Sciences and Engineering Division, Pro-QM EFRC (DE-SC0019443). Z.Z. and C.F. were supported by the Ministry of Science and Technology of China under Grant No. 2016YFA0302400, National Science Foundation of China under Grant No. 11674370, and Chinese Academy of Sciences under Grants No. XXH13506-202 and No. XDB33000000. A.A. was supported by the Gordon and Betty Moore Foundation EPiQS Initiative through Grants No. GBMF 4305 and No. GBMF 8691 at the University of Illinois.

[1] J. von Neumann and E. Wigner, On the behavior of eigenvalues in adiabatic processes, Phys. Z. **30**, 467 (1929).

[2] E. Teller, The crossing of potential surfaces, J. Phys. Chem. **41**, 109 (1937).

[3] M. V. Berry, Semiclassical mechanics of regular and irregular motion, in *Les Houches Lecture Series, Session XXXVI*, edited by G. Iooss, R. H. G. Helleman, and R. Strora (North-Holland, Amsterdam, 1983), pp. 171–271.

[4] M. V. Berry and M. Wilkinson, Diabolical points in the spectra of triangles, Proc. R. Soc. London, Ser. A **392**, 15 (1984).

[5] W. Hamilton, Third supplement to an essay on the theory of systems of rays, Trans. R. Irish Acad. **17**, 1 (1837).

[6] M. Berry and M. Jeffrey, Conical diffraction: Hamilton's diabolical point at the heart of crystal optics, in *Progress in Optics*, edited by E. Wolf (Elsevier, Amsterdam, 2007), Vol. 50, pp. 13–50.

[7] M. V. Berry and M. R. Dennis, The optical singularities of birefringent dichroic chiral crystals, Proc. R. Soc. London Ser. A **459**, 1261 (2003).

[8] G. Herzberg and H. C. Longuet-Higgins, Intersection of potential energy surfaces in polyatomic molecules, Discuss. Faraday Soc. **35**, 77 (1963).

[9] C. A. Mead and D. G. Truhlar, On the determination of Born-Oppenheimer nuclear motion wave functions including complications due to conical intersections and identical nuclei, J. Chem. Phys. **70**, 2284 (1979).

[10] L. S. Cederbaum, R. S. Friedman, V. M. Ryaboy, and N. Moiseyev, Conical Intersections and Bound Molecular States Embedded in the Continuum, Phys. Rev. Lett. **90**, 013001 (2003).

[11] A. Farhan, L. Canto, J. Rasmussen, and P. Ring, Form factors for two-nucleon transfer in the diabolical region of rotating nuclei, Nucl. Phys. A **597**, 387 (1996).

[12] A. Ferretti, A. Lami, and G. Villani, Transition probability due to a conical intersection: On the role of the initial conditions and of the geometric setup of the crossing surfaces, J. Chem. Phys. **111**, 916 (1999).

[13] H. Nielsen and M. Ninomiya, The Adler-Bell-Jackiw anomaly and Weyl fermions in a crystal, Phys. Lett. B **130**, 389 (1983).

[14] P. Hořava, Stability of Fermi Surfaces and *K* Theory, Phys. Rev. Lett. **95**, 016405 (2005).

[15] K. S. Novoselov, A. K. Geim, S. V. Morozov, D. Jiang, M. I. Katsnelson, I. V. Grigorieva, S. V. Dubonos, and A. A. Firsov, Two-dimensional gas of massless Dirac fermions in graphene, Nature (London) **438**, 197 (2005).

[16] X. Wan, A. M. Turner, A. Vishwanath, and S. Y. Savrasov, Topological semimetal and Fermi-arc surface states in the electronic structure of pyrochlore iridates, Phys. Rev. B **83**, 205101 (2011).

[17] G. B. Halasz and L. Balents, Time-reversal invariant realization of the Weyl semimetal phase, Phys. Rev. B **85**, 035103 (2012).

[18] A. A. Soluyanov, D. Gresch, Z. Wang, Q. Wu, M. Troyer, X. Dai, and B. A. Bernevig, Type-II Weyl semimetals, Nature (London) **527**, 495 (2015).

[19] C. L. Kane and E. J. Mele, Quantum Spin Hall Effect in Graphene, Phys. Rev. Lett. **95**, 226801 (2005).

[20] L. Fu, C. L. Kane, and E. J. Mele, Topological Insulators in Three Dimensions, Phys. Rev. Lett. **98**, 106803 (2007).

[21] J. E. Moore and L. Balents, Topological invariants of time-reversal-invariant band structures, Phys. Rev. B **75**, 121306(R) (2007).

[22] R. Roy, Topological phases and the quantum spin Hall effect in three dimensions, Phys. Rev. B **79**, 195322 (2009).

[23] L. D. Landau and E. M. Lifshitz, *Quantum Mechanics* (Elsevier, Singapore, 2007).

[24] M. V. Berry, Quantal phase factors accompanying adiabatic changes, Proc. R. Soc. London Ser. A **392**, 45 (1984).

[25] L. Onsager, Interpretation of the de Haas–van Alphen effect, Philos. Mag. **43**, 1006 (1952).

[26] L. M. Lifshitz and A. Kosevich, On the theory of the de Haas–van Alphen effect for particles with an arbitrary dispersion law, Dokl. Akad. Nauk SSSR **96**, 963 (1954).

[27] L. M. Roth, Semiclassical theory of magnetic energy levels and magnetic susceptibility of Bloch electrons, Phys. Rev. **145**, 434 (1966).

[28] J. B. Keller, Corrected Bohr-Sommerfeld quantum conditions for nonseparable systems, Ann. Phys. (NY) **4**, 180 (1958).

[29] G. P. Mikitik and Y. V. Sharlai, Manifestation of Berry's Phase in Metal Physics, Phys. Rev. Lett. **82**, 2147 (1999).

[30] M.-C. Chang and Q. Niu, Berry phase, hyperorbits, and the Hofstadter spectrum: Semiclassical dynamics in magnetic Bloch bands, Phys. Rev. B **53**, 7010 (1996).

[31] M. H. Cohen and L. M. Falicov, Magnetic Breakdown in Crystals, Phys. Rev. Lett. **7**, 231 (1961).

[32] M. Y. Azbel, Quasiclassical quantization in the neighborhood of singular classical trajectories, J. Exp. Theor. Phys. **12**, 891 (1961).

[33] E. I. Blount, Bloch electrons in a magnetic field, Phys. Rev. **126**, 1636 (1962).

[34] A. B. Pippard, Quantization of coupled orbits in metals, Proc. R. Soc. London Ser. A **270**, 1 (1962).

[35] W. G. Chambers, Magnetic breakdown: Effective hamiltonian and de Haas–van Alphen effect, Phys. Rev. **149**, 493 (1966).

[36] A. A. Burkov, M. D. Hook, and L. Balents, Topological nodal semimetals, Phys. Rev. B **84**, 235126 (2011).

[37] Y. Chen, Y. Xie, S. A. Yang, H. Pan, F. Zhang, M. L. Cohen, and S. Zhang, Nanostructured carbon allotropes with Weyl-like loops and points, Nano Lett. **15**, 6974 (2015).

[38] T. Bzdušek, Q. Wu, A. Rüegg, M. Sigrist, and A. A. Soluyanov, Nodal-chain metals, Nature (London) **538**, 75 (2016).

[39] C.-K. Chiu and A. P. Schnyder, Classification of reflection-symmetry-protected topological semimetals and nodal superconductors, Phys. Rev. B **90**, 205136 (2014).

[40] B.-J. Yang, T. A. Bojesen, T. Morimoto, and A. Furusaki, Topological semimetals protected by off-centered symmetries in nonsymmorphic crystals, Phys. Rev. B **95**, 075135 (2017).

[41] C. Fang, H. Weng, X. Dai, and Z. Fang, Topological nodal line semimetals, Chin. Phys. B **25**, 117106 (2016).

[42] R. Peierls, Zur theorie des diamagnetismus von leitungselektronen, Z. Phys. **80**, 763 (1933).

[43] J. M. Luttinger, The effect of a magnetic field on electrons in a periodic potential, Phys. Rev. **84**, 814 (1951).

[44] C. Zener and R. H. Fowler, Non-adiabatic crossing of energy levels, Proc. R. Soc. London Ser. A **137**, 696 (1932).

[45] A. Slutskin, Dynamics of conduction electrons under magnetic breakdown conditions, J. Exp. Theor. Phys. **26**, 474 (1968).

[46] M. Kaganov and A. Slutskin, Coherent magnetic breakdown, Phys. Rep. **98**, 189 (1983).

[47] T. E. O'Brien, M. Diez, and C. W. J. Beenakker, Magnetic Breakdown and Klein Tunneling in a Type-II Weyl Semimetal, Phys. Rev. Lett. **116**, 236401 (2016).

[48] A. Alexandradinata and L. Glazman, Geometric Phase and Orbital Moment in Quantization Rules for Magnetic Breakdown, Phys. Rev. Lett. **119**, 256601 (2017).

[49] A. Alexandradinata and L. Glazman, Semiclassical theory of Landau levels and magnetic breakdown in topological metals, Phys. Rev. B **97**, 144422 (2018).

[50] C. Wang, W. Duan, L. Glazman, and A. Alexandradinata, Landau quantization of nearly degenerate bands and full symmetry classification of Landau level crossings, Phys. Rev. B **100**, 014442 (2019).

[51] M. Breitkreiz, N. Bovenzi, and J. Tworzydło, Phase shift of cyclotron orbits at type-I and type-II multi-Weyl nodes, Phys. Rev. B **98**, 121403(R) (2018).

[52] G. E. Zil'berman, Behavior of an electron in a periodic electric and a uniform magnetic field, J. Exp. Theor. Phys. **5**, 208 (1957).

[53] A. Alexandradinata and J. Höller, No-go theorem for topological insulators and high-throughput identification of Chern insulators, Phys. Rev. B **98**, 184305 (2018).

[54] D. Shoenberg, *Magnetic Oscillations in Metals* (Cambridge University Press, Cambridge, UK, 1984).

[55] J. S. Dhillon and D. Shoenberg, The de Haas–van Alphen effect III. Experiments at fields up to 32KG, Philos. Trans. R. Soc. London Ser. A **248**, 1 (1955).

[56] C. Guo, A. Alexandradinata, C. Putzke, F.-R. Fan, S. Zhang, Q. Wu, O. V. Yazyev, K. R. Shirer, M. D. Bachmann, E. D. Bauer, F. Ronning, C. Felser, Y. Sun, and P. J. W. Moll, Temperature dependence of quantum oscillations from non-parabolic dispersions, Nat. Commun. **12**, 6213 (2021).

[57] Q. Xu, R. Yu, Z. Fang, X. Dai, and H. Weng, Topological nodal line semimetals in the CaP_3 family of materials, Phys. Rev. B **95**, 045136 (2017).

[58] Y. Quan, Z. P. Yin, and W. E. Pickett, Single Nodal Loop of Accidental Degeneracies in Minimal Symmetry: Triclinic $CaAs_3$, Phys. Rev. Lett. **118**, 176402 (2017).

[59] L. S. Xie, L. M. Schoop, E. M. Seibel, Q. D. Gibson, W. Xie, and R. J. Cava, A new form of Ca_3P_2 with a ring of dirac nodes, APL Mater. **3**, 083602 (2015).

[60] Y.-H. Chan, C.-K. Chiu, M. Y. Chou, and A. P. Schnyder, Ca_3P_2 and other topological semimetals with line nodes and drumhead surface states, Phys. Rev. B **93**, 205132 (2016).

[61] W. Dahlmann and H. G. v. Schnering, CaP_3, ein neues calciumphosphid, Naturwissenschaften **60**, 518 (1973).

[62] See Supplemental Material, which cites Refs. [23,25,27–29,44,46,49,50,54,57,64,64,65,65,77–88], at http://link.aps.org/supplemental/10.1103/PhysRevB.105.045141 for more details about angle-dependent ultrasonic attenuation, quantization rules, effective mass model of candidate materials, and a discussion about coexisting Fermi pockets.

[63] A. M. Toxen and S. Tansal, Giant oscillations in the magnetoacoustic attenuation of bismuth, Phys. Rev. **137**, A211 (1965).

[64] Y. Shapira, Acoustic wave propagation in high magnetic fields, in *Principles and Methods*, Physical Acoustics Vol. 5, edited by W. P. Mason (Academic Press, San Diego, 1968), pp. 1–58.

[65] V. L. Gurevich, V. G. Skobov, and Y. A. Firsov, Giant quantum oscillations in the acoustical absorption by a metal in a magnetic field, J. Exp. Theor. Phys. **13**, 552 (1961).

[66] P. J. Moll, Focused ion beam microstructuring of quantum matter, Annu. Rev. Condens. Matter Phys. **9**, 147 (2018).

[67] W. Zawadzki, Intraband and interband magneto-optical transitions in semiconductors, in *Landau Level Spectroscopy*, edited by G. Landwehr and E. I. Rashba (Elsevier, North-Holland, Amsterdam, 1991), p. 485.

[68] M. A. Ordal, R. J. Bell, R. W. Alexander, L. L. Long, and M. R. Querry, Optical properties of Au, Ni, and Pb at submillimeter wavelengths, Appl. Opt. **26**, 744 (1987).

[69] H.-J. Hagemann, W. Gudat, and C. Kunz, Optical constants from the far infrared to the x-ray region: Mg, Al, Cu, Ag, Au, Bi, C, and Al_2O_3, J. Opt. Soc. Am. **65**, 742 (1975).

[70] D. Grischkowsky, S. Keiding, M. van Exter, and C. Fattinger, Far-infrared time-domain spectroscopy with terahertz beams of dielectrics and semiconductors, J. Opt. Soc. Am. B **7**, 2006 (1990).

[71] Optical data and references are available at https://refractiveindex.info.

[72] J. Li, L.-X. Zhao, Y.-Y. Wang, X.-M. Wang, C.-Y. Ma, W.-L. Zhu, M.-R. Gao, S. Zhang, Z.-A. Ren, and G.-F. Chen, Transport properties of topological nodal-line semimetal candidate $CaAs_3$ under hydrostatic pressure, Chin. Phys. B **28**, 046202 (2019).

[73] S. Li, Z. Guo, D. Fu, X.-C. Pan, J. Wang, K. Ran, S. Bao, Z. Ma, Z. Cai, R. Wang, R. Yu, J. Sun, F. Song, and J. Wen, Evidence for a Dirac nodal-line semimetal in $SrAs_3$, Sci. Bull. **63**, 535 (2018).

[74] L. An, X. Zhu, W. Gao, M. Wu, W. Ning, and M. Tian, Chiral anomaly and nontrivial Berry phase in the topological nodal-line semimetal $SrAs_3$, Phys. Rev. B **99**, 045143 (2019).

[75] M. M. Hosen, G. Dhakal, B. Wang, N. Poudel, K. Dimitri, F. Kabir, C. Sims, S. Regmi, K. Gofryk, D. Kaczorowski, A. Bansil, and M. Neupane, Experimental observation of drumhead surface states in $SrAs_3$, Sci. Rep. **10**, 2776 (2020).

[76] S. Pezzini, M. Van Delft, L. Schoop, B. Lotsch, A. Carrington, M. Katsnelson, N. Hussey, and S. Wiedmann, Unconventional mass enhancement around the Dirac nodal loop in ZrSiS, Nat. Phys. **14**, 178 (2018).

[77] A. I. Akhiezer, M. I. Kaganov, and G. L. Liubarskii, Ultrasonic absorption in metals, J. Exp. Theor. Phys. **5**, 685 (1957).

[78] Y. Sawada, E. Burstein, and L. Testardi, Determination of the Energy Band Parameters of Bismuth by Giant Quantum Attenuation of Sound Waves, in *Proceedings of the International Conference on the Physics of Semiconductors, Kyoto, 1966* (Physical Society of Japan, 1966).

[79] N. W. Ashcroft and N. D. Mermin, *Solid State Physics* (Thomson Learning, Boston, MA, 1976).

[80] V. G. Skobov, Quantum theory of sound absorption by metals in a magnetic field, J. Exp. Theor. Phys. **13**, 1014 (1961).

[81] L. M. Lifshitz and A. Kosevich, Theory of magnetic susceptibility in metals at low temperatures, J. Exp. Theor. Phys. **2**, 636 (1956).

[82] L. M. Falicov and H. Stachowiak, Theory of the de Haas–van Alphen effect in a system of coupled orbits. application to magnesium, Phys. Rev. **147**, 505 (1966).

[83] J. Zak, Magnetic translation group, Phys. Rev. **134**, A1602 (1964).

[84] E. Brown, Bloch electrons in a uniform magnetic field, Phys. Rev. **133**, A1038 (1964).

[85] J. P. Perdew, K. Burke, and M. Ernzerhof, Generalized Gradient Approximation Made Simple, Phys. Rev. Lett. **77**, 3865 (1996).

[86] J. Heyd, G. E. Scuseria, and M. Ernzerhof, Hybrid functionals based on a screened Coulomb potential, J. Chem. Phys. **118**, 8207 (2003).

[87] G. Kresse and J. Furthmüller, Efficient iterative schemes for *ab initio* total-energy calculations using a plane-wave basis set, Phys. Rev. B **54**, 11169 (1996).

[88] G. Kresse and D. Joubert, From ultrasoft pseudopotentials to the projector augmented-wave method, Phys. Rev. B **59**, 1758 (1999).